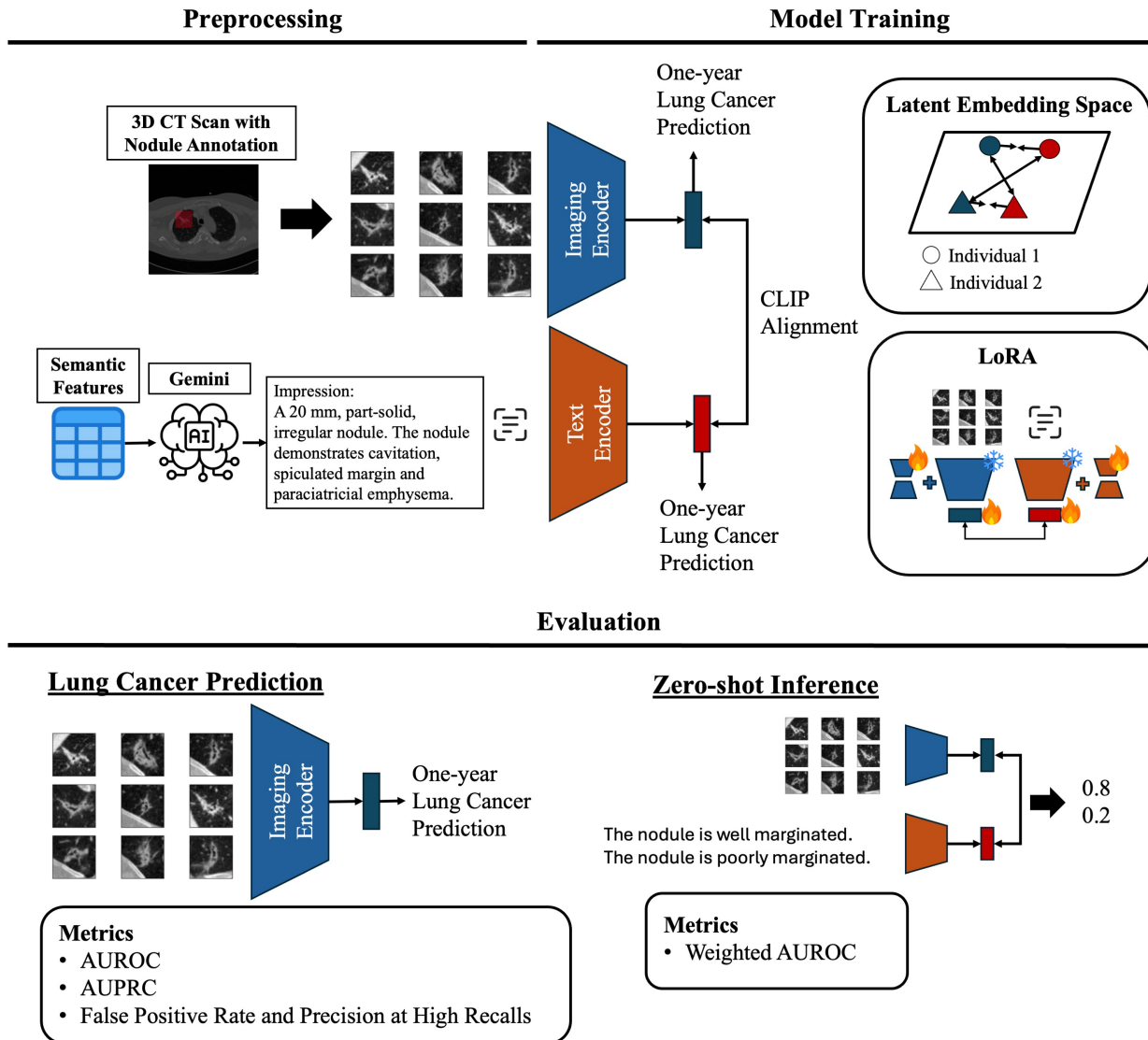


Graphical Abstract

Vision-Language Model-Based Semantic-Guided Imaging Biomarker for Early Lung Cancer Detection

Luoting Zhuang, Seyed Mohammad Hossein Tabatabaei, Ramin Salehi-Rad, Linh M. Tran, Denise R. Aberle, Ashley E. Prosper, William Hsu



Vision-Language Model-Based Semantic-Guided Imaging Biomarker for Early Lung Cancer Detection

Luoting Zhuang^a, Seyed Mohammad Hossein Tabatabaei^a, Ramin Salehi-Rad^b, Linh M. Tran^b, Denise R. Aberle^a, Ashley E. Prosper^a, William Hsu^{a,*}

^a*Medical & Imaging Informatics, Department of Radiological Sciences, David Geffen School of Medicine at UCLA, Los Angeles, 90095, CA, USA*

^b*Department of Medicine, Division of Pulmonology and Critical Care, David Geffen School of Medicine at UCLA, Los Angeles, 90095, CA, USA*

Abstract

Objective: A number of machine learning models have utilized semantic features, deep features, or both to assess lung nodule malignancy. However, their reliance on manual annotation during inference, limited interpretability, and sensitivity to imaging variations hinder their application in real-world clinical settings. Thus, this research aims to integrate semantic features derived from radiologists' assessments of nodules, allowing the model to learn clinically relevant, robust, and explainable features for predicting lung cancer.

Methods: We obtained 938 low-dose CT scans from the National Lung Screening Trial with 1,246 nodules and semantic features. Additionally, the Lung Image Database Consortium dataset contains 1,018 CT scans, with 2,625 lesions annotated for nodule characteristics. Three external datasets were obtained from UCLA Health, the LUNGx Challenge, and the Duke Lung Cancer Screening. For imaging input, we obtained 2D nodule slices from nine directions from $50 \times 50 \times 50$ mm nodule crop. We converted structured semantic features into sentences using Gemini. We finetuned a pretrained Contrastive Language-Image Pretraining model with a parameter-efficient fine-tuning approach to align imaging and semantic features and predict the one-year lung cancer diagnosis.

Results: We evaluated the performance of the one-year diagnosis of lung cancer with AUROC and AUPRC and compared it to three state-of-the-art models. Our model demonstrated an AUROC of 0.90 and AUPRC of 0.78, outperforming baseline state-of-the-art models on external datasets. Using CLIP, we also obtained predictions on semantic features, such as nodule margin (AUROC: 0.81), nodule consistency (0.81), and pleural attachment (0.84), that can be used to explain model predictions.

Conclusion: Our approach accurately classifies lung nodules as benign or malignant, providing explainable outputs, aiding clinicians in comprehending the underlying meaning of model predictions. This approach also prevents the model from learning shortcuts and generalizes across clinical settings.

Keywords: Lung Cancer Early Detection, Computed Tomography, Vision-Language Model, Semantic Features

*Corresponding author

1. Introduction

Lung cancer remains the leading cause of cancer-related deaths [1, 2]. Computed tomography (CT) has demonstrated efficacy in the detection of lung cancer and in decreasing cancer-related mortality during lung cancer screening or incidentally within routine health-care settings [3, 4]. However, radiologists are experiencing burnout with the increasing application of CT and the growing number of detected nodules [5]. Computer-aided diagnostic systems have been proposed to alleviate the workload of radiologists by providing an accurate lung cancer prediction based on patients' data automatically.

Traditional machine learning models in lung nodule risk assessment focus on semantic features, deep features, or both. Semantic features refer to the descriptive terms radiologists use to characterize regions of interest, such as their shape, margin, vascularity, and other attributes. Models trained on semantic features are usually easier to interpret, but they also introduce difficulties when scaled for clinical use, as they require manual annotation from radiologists [6, 7]. Recently, deep learning has become a powerful tool in lung cancer risk assessment due to its strong capability of extracting complex features from CT without any manual input [8, 9]. While imaging-based models have demonstrated impressive performance, they still encounter numerous obstacles. For instance, imaging features are sensitive to variations in the acquisition and reconstruction of CT scans, including dose levels, slice thicknesses, and reconstruction kernels [10, 11]. Moreover, research has indicated that deep learning models learn shortcuts: characteristics highly correlated with outcomes but lack clinical significance in medical imaging [12, 13]. This phenomenon could adversely impact the reproducibility of features and the performance of models. Additionally, the lack of explainability remains one of the major challenges related to deep features. Heatmaps or attribution maps generated by explainability methods, such as GradCAM [14], can not clarify the feature the model focuses on.

Combining these features has become more popular for enhancing lung cancer prediction performance. However, directly merging two features often reduces applicability in clinical settings, as manual annotation remains necessary. Alternative approaches tackle this problem through co-learning and multi-task learning [15, 16, 17], but these models face challenges regarding explainability or training difficulties when dealing with numerous semantic features. An emerging approach in vision-language models (VLM), Contrastive Language-Image Pretraining (CLIP) [18], addresses this gap by learning the alignment between imaging features and descriptive text. Guided by text, these models allow deep visual features to capture a richer and more robust representation. Therefore, in this study, we have made the following key contributions:

1. We employed CLIP to include the semantic features to direct the model in obtaining clinically significant and robust features for the prediction of lung cancer.
2. We curated a unique dataset comprising CT scans and their corresponding semantic features, which were annotated by radiologists. The semantic features encompass nodule characteristics as well as characteristics of the surrounding environment.
3. We benchmarked our CLIP model against several state-of-the-art (SOTA) lung cancer prediction models. Our model demonstrated better and more robust results in external datasets that include CT scans collected from different clinical scenarios (e.g., screening

and routine clinical care) and different types of CT scans (e.g., low-dose CT, diagnostic CT, and contrast-enhanced CT).

4. We explored the zero-shot inference, a feature of CLIP-based models that generates semantic features despite not being explicitly trained to do so.
5. Several adjustments were introduced to accommodate CLIP fine-tuning on 3D images with limited data. By combining these strategies with extensive domain knowledge, our model shows comparable and better performance than imaging-based models trained on tens of thousands of cases using an order of magnitude fewer cases.

Statement of Significance

Problem or Issue	Current imaging-based lung nodule malignancy models lack explainability and are prone to learning shortcuts, which limits their generalizability and applicability in diverse clinical settings.
What is Already Known	Vision-language models, especially CLIP, effectively integrate information from images and texts by aligning paired image and text features within a shared embedding space. Its zero-shot inference capability enhances the model’s explainability, allowing predictions on tasks for which it is not explicitly trained.
What this Paper Adds	This paper utilizes CLIP to incorporate semantic features that guide the imaging model to learn clinically relevant and reliable imaging biomarkers of malignancy, aiming to improve lung cancer classification across diverse patient populations and CT acquisition protocols. This model offers explainability, using semantic features to explain model predictions to radiologist end users.
Who would Benefit	This work benefits radiologists by offering a reliable and interpretable tool for predicting lung cancer risk, aiding in the early detection, and enabling timely diagnosis and treatment for patients.

2. Related Work

2.1. Imaging-based Lung Cancer Prediction Model

CT scans have been utilized to train deep learning models, and these models have also been made available online for potential implementation in real-world clinical settings. Sybil [8] is a publicly available deep learning model that employs ResNet18 to predict lung cancer risk scores for up to six years using low-dose CT (LDCT) scans. Sybil was trained utilizing the NLST dataset, with around 15,000 CT scans, and has demonstrated consistently robust performance during external validation using screening scans from two distinct sites. Notably, Sybil takes the entire CT scan instead of the nodule region. An attention mechanism was integrated to enhance Sybil’s focus on the nodule.

In another study, Venkadesh et al. [9] developed a model to predict the malignancy risk of pulmonary nodules by integrating ResNet18 for 2D nodule crops and Inception-V1 for 3D

nodule crops. This model was trained using 16,077 nodules from the NLST dataset and has shown robust performance in the external cancer screening datasets.

Although these models have shown effectiveness in predicting lung cancer, they still lack explainability. It is unclear what features have been captured from the image. Moreover, as these models were trained on NLST data, there is a possibility that the models overfit the screening dataset, which comprises only LDCT scans, limiting their applicability across various settings, such as diagnostic CT and contrast-enhanced CT. Studies have also shown that the risk score generated from the Sybil model can be sensitive to the CT reconstruction parameters, such as slice thickness and kernel [10].

2.2. *Imaging Feature Learning Guided by Semantic Features*

Although imaging features play an important role, numerous studies have explored integrating clinical or semantic features to improve lung cancer risk assessment. The model can understand the relationship between imaging and semantic features by including clinical features, making the embedding more clinically relevant and easier to interpret. However, while medical imaging is more readily accessible, semantic features often require labor-intensive annotation by radiologists, which can also exhibit considerable variability. The existing approach of directly fusing two modalities may reduce the model’s practical value in clinical settings and increase radiologists’ workload to provide annotations. Several studies attempted to address the issue through co-learning and multi-task learning.

For example, DeepIPN [16] is a co-learning model trained on 1,284 in-house data, integrating both imaging features and clinical features, which consist of demographics and nodule characteristics. CT features were obtained from the top five most likely nodules based on a nodule detection algorithm. They implemented three prediction branches: one for the imaging feature, one for the clinical tabular feature, and one for the fusion of imaging and clinical features. The model cannot generate explanations of its outputs despite jointly modeling information across two modalities.

Moreover, a hierarchical semantic convolutional neural network (HSCNN) [15] was trained for multi-task learning. This included the low-level task of predicting semantic features and the high-level task of assessing lung cancer risk. The low-level output embeddings were integrated with representations from the global convolutional layers to derive the high-level output. This model is inherently interpretable because it allows us to obtain predictions of semantic features from the low-level task branches. Nevertheless, challenges emerge when numerous semantic features are involved. For instance, tasks may exhibit conflict, resulting in discrepancies in the gradient updating direction within the shared weights, ultimately reducing overall performance.

2.3. *Vision-Language Model*

VLMs have recently become popular, employing deep learning techniques to understand visual and linguistic information concurrently. Generally, joint representations are learned to map features from different modalities into a shared latent space. One of the VLMs is CLIP [18], which aligns natural images with their corresponding captions. It has exhibited exceptional performance across a variety of downstream tasks. This framework has also been successfully applied in the medical field, as clinicians typically generate reports linked

to various medical modalities, such as echocardiograms [19], chest X-rays [20], histopathology images [21], and CT scans [22].

The CLIP framework can also be suitable for predicting lung cancer by aligning nodule-specific features with semantic features. By mapping both types of features from the same individual into a shared embedding space, the image features can incorporate information from the semantic features. Additionally, the model offers greater explainability, as it can perform zero-shot inference to evaluate how closely an image aligns with a given semantic feature. However, several questions arise when training such a contrastive learning model on medical imaging and semantic features. (1) The success of CLIP relies on a large dataset, which can be easily downloaded from online sources. Medical imaging data and reports can also be collected with relative ease. However, obtaining detailed characterization for specific regions, such as nodules, poses significant challenges. Such semantic features generally require annotations from radiologists, resulting in significantly smaller datasets with semantic features. Given these limitations, training a VLM model from scratch appears impractical, necessitating reliance on pretrained encoders from CLIP. However, it is notable that the OpenAI pretrained model has been trained on 2D natural images, whereas medical imaging data is usually in 3D format. (2) Semantic features are typically presented in tabular format and may contain missing values. Tabular data limits the use of the pretrained text encoder from the CLIP model, which already maintains some degree of alignment between images and text.

In a previous study, CLIP-Lung [23] was introduced to utilize CLIP for learning generalized visual representations from semantic features using the LIDC dataset. However, one of the critical limitations of the study is the lack of investigation into one of CLIP’s most distinctive capabilities—zero-shot inference. While CLIP is not trained to predict semantic features, zero-shot inference identifies semantic features most similar to a given imaging feature embedding. Leveraging this could improve model explainability, enhancing radiologists’ trust in the system. Second, the authors did not perform a benchmark to evaluate the model against SOTA lung cancer risk prediction models across datasets with different properties. Additionally, the model made predictions of risk score estimations from radiologists instead of the biopsy-confirmed results. Furthermore, the model was trained on a limited number of semantic features that do not fully characterize the properties of the nodule and the surrounding areas.

3. Methods

3.1. Datasets

3.1.1. Training Data

The training data were collected from two publicly available datasets (Table 1). First, we obtained 938 LDCT scans containing at least one nodule from the National Lung Screening Trial (NLST) [3]. We acquired a unique dataset with thorough annotations performed by radiologists at UCLA Health. They annotated the nodule’s location and curated a holistic set of 19 semantic features, listed in Table S1, for a total of 1,246 nodules [24]. These features encompass general features, such as shape, margin, consistency, and internal characteristics like necrosis and cyst-like spaces, alongside external features, including vascular convergence

Table 1: **Datasets.** The datasets employed in this study are summarized with respect to cohort size, proportion of lung cancer cases, imaging modality, and data source. It is important to note that the biopsy-confirmed diagnosis for lung cancer in the LIDC dataset are incomplete.

Dataset	N (% positive)	CT	Patient Cohort
Training Datasets			
National Lung Screening Trial	938 (23%)	Low-dose	Screening
Lung Image Database Consortium	1,018 (9%)	Low-dose and Diagnostic	Screening & Incidental
External Datasets			
LUNGx Challenge	70 (50%)	Diagnostic & Contrast-enhanced	Incidental
UCLA Health	51 (55%)	Diagnostic & Low-dose	Incidental
Duke Lung Cancer Screening	1,120 (5.6%)	Low-dose	Screening

and emphysema. Additionally, the Lung Image Database Consortium (LIDC) dataset contains both diagnostic and screening CT scans from 1,018 cases, with 2,625 lesions annotated for subjective nodule characteristics, including sphericity, lobulation, consistency, internal structure, margin, and spiculation [25]. Since multiple radiologists annotated the nodules in the studies, and their annotations varied, we used a majority vote at the pixel level for the nodule annotations and took the median of the semantic feature scores.

3.1.2. External Data

We collected three external datasets featuring unique patient cohorts and CT types. First, we obtained 51 CT scans from UCLA Health, collected retrospectively from routine clinical settings. This dataset includes a unique subset of patients, including individuals who have self-reported as never-smoked with incidental pulmonary nodules and do not meet the eligibility criteria for lung cancer screening. All individuals underwent biopsy, indicating a relatively higher-risk patient cohort. Radiologists at UCLA Health annotated the locations of the most suspicious nodules. Second, we curated the publicly accessible LUNGx Challenge dataset, containing 70 diagnostic and contrast-enhanced diagnostic CTs with 83 annotated nodules [26]. Lastly, the Duke Lung Cancer Screening (DLCS) dataset consists of scans from a screening process and includes 1,120 LDCT scans with 2,487 nodules, all annotated with their internal nodule detection algorithm [27]. In addition, these three datasets have different lung cancer distributions. The LUNGx and UCLA datasets exhibit a generally balanced distribution of malignant and benign cases, with malignant cases comprising 50% (35 cases) and 55% (28 cases) in each dataset, respectively. In contrast, only 5.6% (63 cases) are diagnosed as lung cancer in the DLCS dataset.

3.2. Data Preprocessing

3.2.1. Semantic feature preprocessing

Directly aligning tabular semantic and imaging features using the CLIP framework poses numerous difficulties. Firstly, given the limited training data compared to the quantity typically employed in contrastive learning and the training of the CLIP model, it is beneficial to utilize the pre-trained CLIP model, which already exhibits a certain degree of alignment between image features and text features. Secondly, tabular data typically contains numerous missing values. Similarly, radiologists at UCLA overlooked some semantic features for

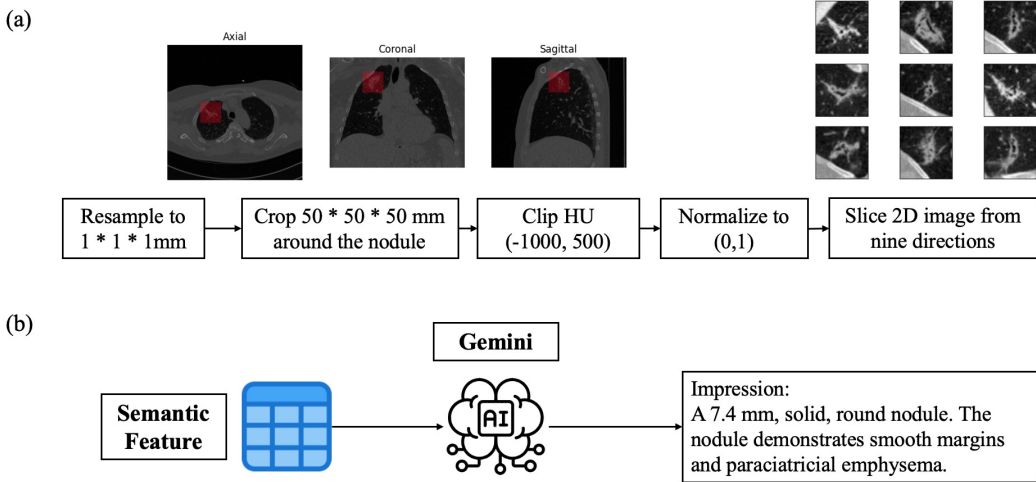


Figure 1: **CT and Semantic Features Preprocessing Steps.** (a) For the CT scan, we resampled the image to a standard spacing of $1 \times 1 \times 1$ mm and positioned a bounding box of size 50mm around the nodule. The Hounsfield Unit values were clipped between -1000 and 500, then normalized to a scale of 0 to 1. We sliced the nodule from nine different angles to accommodate the CLIP architecture while preserving most nodule structures. (b) For semantic features, we input the feature into Gemini with a prompt designed to generate text similar to a radiology report.

specific cases in NLST during annotation. Furthermore, the NLST and LIDC datasets comprise distinct sets of semantic features, thus complicating the harmonization of the tabular semantic features. Consequently, we proposed a workaround to convert semantic features into text to resolve the challenge above. First, we consulted with radiologists to standardize the semantic features by aligning the terms between the two datasets as closely as possible. We treated features that appear in NLST but not in LIDC as missing values. Second, we converted semantic features into radiology report-like text using Gemini [28], a large language model developed by Google DeepMind (Fig. 1b). It allows merging datasets with missing values and mismatched semantic features. Furthermore, we implemented natural language preprocessing augmentation to substitute the text with synonyms, allowing for greater variation during training.

3.2.2. CT images preprocessing

Fig. 1a illustrates the CT preprocessing pipeline. First, we standardized and resampled all the 3D CT images to a spatial resolution of $1 \times 1 \times 1$ mm. Based on the annotated nodule mask or the nodule’s location, we placed a $50 \times 50 \times 50$ mm bounding box around the nodule. Furthermore, we clipped the Hounsfield Unit (HU) values within the range of -1000 to 500 and normalized them to the range (0, 1). Since we aimed to use the CLIP model, which had been pretrained on 2D natural images by OpenAI, we converted the 3D patch containing the nodule into 2D images across nine different planes, all passing through the nodule centroid. By doing so, the image encoder can capture nodule information in 2.5D, providing additional

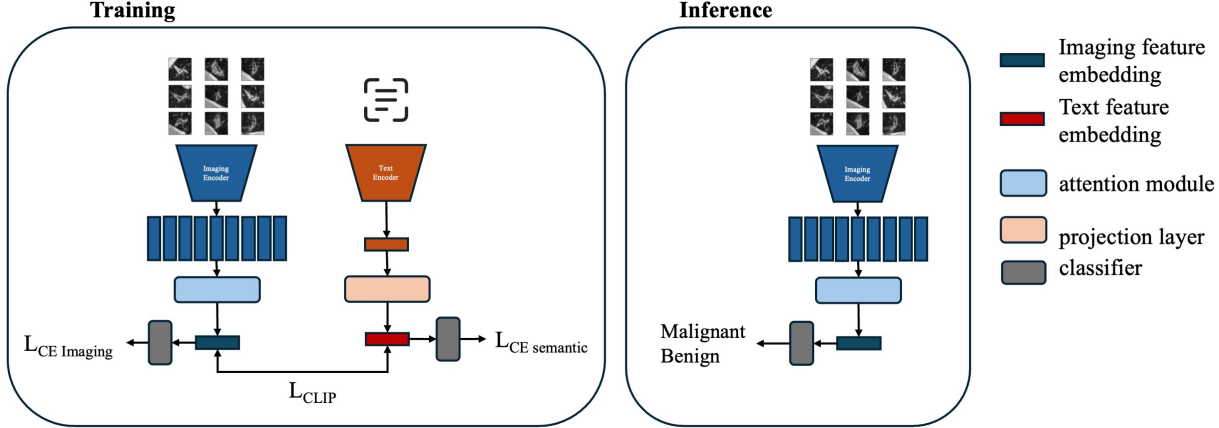


Figure 2: **CLIP Model Architecture.** The pre-trained CLIP was fine-tuned to pull the paired imaging and semantic features close together, which allowed the model to learn meaningful relationships between imaging features and semantic features. During training, nodule images sliced from nine different directions of 3D nodule crops were passed into the vision transformer image encoder. The attention-based multiple-instance learning module aggregated the output imaging features to obtain a single embedding. The sentence containing the semantic features was passed into the text encoder to generate the text feature embedding. The visual and text features were then aligned using CLIP loss. Two prediction heads were independently attached after the encoders to predict the 1-year lung cancer risk. During inference, only the imaging feature was required, allowing it to be applied universally without the need for a radiologist’s evaluation on CT.

details about the nodule than a single 2D slice. This is important for characterizing nodules because different areas of the nodule can show various attributes. Thus, this method not only fulfills the model input criteria but also maintains as much 3D structural information as possible. Prior to inputting the 2.5D images into the image encoder, we normalized the 2D image again using CLIP preprocessing to maintain consistency with the pretrained model’s input requirements.

3.3. Experimental Setup

The architectural framework of the model is illustrated in Figure 1. The CLIP model was initialized using the weights from OpenAI’s CLIP (ViT-B32) and was subsequently fine-tuned to align imaging and semantic features. The 2.5D images were processed through the image encoder, and an attention-based multiple instance learning model was employed to generate the attention scores and aggregate features across nine 2D images [29]. Simultaneously, we provided Gemini-generated radiology report-like text to the text encoder to obtain feature embeddings. During training, samples were selected based on the frequency of their semantic features: nodules with rare features were chosen more often to increase contrast within each batch. Two projection heads were attached after each encoder to transform the features into 256-dimensional feature embeddings, which were aligned with two InfoNCE losses [30]:

$$\mathcal{L}_{\text{InfoNCE-Image}} = -\frac{1}{B} \sum_{i=1}^B \log \left(\frac{\exp(\text{sim}(I_i, S_i)/\tau)}{\sum_{j=1}^B \exp(\text{sim}(I_i, S_j)/\tau)} \right) \quad (1)$$

$$\mathcal{L}_{\text{InfoNCE-semantic}} = -\frac{1}{B} \sum_{i=1}^B \log \left(\frac{\exp(\text{sim}(I_i, S_i)/\tau)}{\sum_{k=1}^B \exp(\text{sim}(I_k, S_i)/\tau)} \right) \quad (2)$$

$$\mathcal{L}_{\text{CLIP}} = \frac{1}{2} (\mathcal{L}_{\text{InfoNCE-Image}} + \mathcal{L}_{\text{InfoNCE-semantic}}) \quad (3)$$

where I_i and S_i represent a pair of images and their corresponding semantic features from nodule i , which we consider a positive pair. The negative pairs are imaging I_i and all other semantic features in the batches of size B , S_j , where $j \neq i$. In addition, negative pairs also include semantic features S_i and all other imaging I_k . The cosine similarity is computed for positive and negative pairs, and softmax is used to transform the similarity into probability, which indicates how likely each imaging and semantic feature is in the positive pair. The temperature, τ , is a trainable parameter to control the smoothness of the output probability.

This framework enabled the image encoder to learn enriched, clinically relevant insights from semantic features and can generate more robust imaging features that emphasize regions corresponding to radiologist-interpretable features rather than spurious correlations. However, the limited training data can lead to a suboptimal alignment between the two modalities. Therefore, we proposed adding two prediction branches, which predict the one-year lung cancer diagnoses based on the imaging and semantic text features. It will allow the model to learn features more relevant to lung cancer diagnosis while aligning the two feature sets. The prediction branch was trained with cross-entropy loss. In addition to the prediction branches, we utilized Low-Rank Adaptation (LoRA), a parameter-efficient technique that resulted in only 0.4% of the trainable parameters, effectively preventing overfitting [31]. Specifically, low-rank matrices were incorporated into each Q, K, and V layer of the vision and text transformer. The final weights were obtained by summing the pretrained weights with the low-rank matrices. The pretrained weights were kept frozen throughout training, and only the low-rank matrices were updated.

The model was trained with three losses: CLIP loss (InfoNCE loss) and two cross-entropy losses, using equal weights and an AdamW optimizer with a learning rate of 0.0001 and a weight decay of 0.1. In LoRA, we set the rank of the inserted matrices to 2, the scale factor to 1, and the dropout rate to 0.25.

3.4. Evaluation

We selected 20% of nodules from NLST as the held-out test set. The rest of the nodules from NLST were combined with LIDC data for training. We performed 5-fold cross-validation with 80% and 20% split on the patient level. We selected the best hyperparameters based on the mean validation results. Similar to Sybil [8], we adopted an ensemble approach for inference by averaging the predictions from all five trained models. Since each individual can have multiple nodules, we took the maximum risk score to represent the patient-level risk score.

We evaluated the model's performance in predicting lung cancer risk within one year using the Area Under the Receiver Operating Characteristic (AUROC) and the Area Under the Precision-Recall Curve (AUPRC). High sensitivity in lung cancer screening is essential to detect malignant nodules early, so patients receive a timely diagnosis. Since both AUROC and AUPRC capture the trade-off between recall and false positive rate (FPR) or precision

across all thresholds, areas corresponding to low recall may be less relevant for our analysis, especially in lung cancer screening datasets, such as NLST and DLCS. Therefore, we also computed the FPR and precision at recall levels approximating 0.6, 0.7, 0.8, and 0.9. This allows us to assess how well each model minimizes FDR and maximizes precision when aiming to capture as many lung cancer cases as possible.

We compared our model to three SOTA lung cancer risk prediction models, Sybil, Venkadesh et al., and DeepIPN, which were previously introduced in the Related Work section. We input whole CT scans for the Sybil model and obtained the first-year risk score. For DeepIPN, lung cancer risk scores were extracted only from the imaging branch for model comparison. Since the DeepIPN model includes a preprocessing step like lung segmentation, it encountered issues in several instances, which were excluded during the evaluation. In Venkadesh et al., we selected the highest risk score from all patient nodules as the patient’s overall risk score. It is important to note that since Sybil and Venkadesh et al. were both trained on NLST data, there may be issues with data leakage; therefore, we did not evaluate it on the NLST test set. Additionally, the Venkadesh et al. model requires inference to be performed through the Grand Challenge platform, which prevents the evaluation of our in-house UCLA data. The credits available for running inference on the Grand Challenge are limited to obtaining predictions for the DLCS dataset. Consequently, we only acquired the risk scores for the LUNGx dataset.

Most importantly, using CLIP, we also obtained predictions regarding semantic features via zero-shot inference for the NLST test set. For categorical semantic features, we included all possible elements within the sentence "This nodule [margin/shape/consistency/...] is [...]" . For binary semantic features, we use "There is [pleural retraction/cyst-like spaces/...]." to indicate presence and "No findings." to suggest absence. We calculated the cosine similarity between the nodule images and each sentence varying the semantic features that were included in it. The softmax function was applied to the cosine similarity scores. Subsequently, we computed the weighted AUROC score to assess the effectiveness of the zero-shot inference for semantic features with multiple categories and the standard AUROC for those with binary categories.

3.5. Ablation Studies

We performed two experiments to investigate the model’s performance using different tuning methods and modalities.

We experimented with three tuning methods to train the CLIP model (Fig.3). First, fine-tuning involved optimizing all parameters, but this approach is more likely to overfit. Second, in probing, we froze the image and text encoders while training only the projection layers. This can decrease overfitting risk but is less effective in cases of significant domain shifts. For instance, we adapted a model originally trained on RGB natural images and captions to work with grayscale medical images and radiology report-like text. Finally, we employed a parameter-efficient fine-tuning method, called LoRA. Specifically, both image and text encoders remained frozen. The low-rank matrices were inserted into each layer of the encoder. The weights of the encoder and the low-rank matrices were then added to form the final weights for each layer. This approach balances computational efficiency with model adaptation, particularly in domains with limited data.

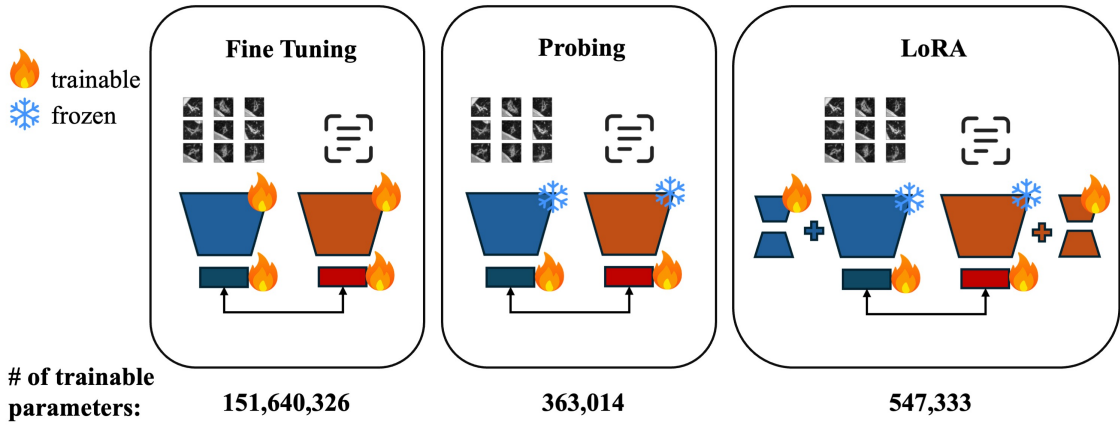


Figure 3: **Different CLIP Tuning Methods.** We examined the training of the CLIP model using three distinct tuning methods as part of our ablation study. All parameters were fine-tuned (left figure). Only two projection layers were fine-tuned (middle figure). A parameter-efficient fine-tuning method called LoRA, which involves inserting trainable low-rank matrices into each layer of the vision and text encoders, was used (right figure). While keeping the pretrained weights frozen, we updated the low-rank matrices. We also allowed the projection layers to be fine-tuned.

To compare the model performance with different modalities, we trained a logistic regression model using the semantic features from the NLST training data and assessed its performance on the NLST test set. Additionally, we trained the model solely with the CLIP vision encoder, using only the imaging data, and evaluated the outcomes on the NLST test set and three external datasets.

We calculated the mean and standard deviation of the AUROC and AUPRC scores for each model across five folds. To evaluate the significance of differences in performance among the three models, we conducted statistical testing utilizing the Friedman Chi-Square test. A post-hoc Nemenyi test was used to obtain the pairwise p-value and assess statistical significance. To compare the two models, we applied the Wilcoxon signed-rank test at a significance level of 0.05.

4. Results

4.1. Lung Cancer Risk Prediction

We present the model performance of 1-year lung cancer prediction with AUROC and AUPRC scores in Table 2. FPR and precision at recall levels approximating 0.6, 0.7, 0.8, and 0.9 are shown in Appendix B.

In the NLST test set, our model surpasses the DeepIPN model, achieving an AUROC of 0.895 and an AUPRC of 0.775. The CLIP model consistently shows favorable FPR and precision scores across four distinct recall levels. When evaluated externally on the LUNGx and UCLA never-smoker cohorts, our model demonstrates superior performance with the following results: for LUNGx, an AUROC of 0.763 and an AUPRC of 0.800, while for UCLA, it achieves an AUROC of 0.768 and an AUPRC of 0.825.

Within the LUNGx cohort, we observe a lower FPR of 0.086 and a higher precision score of 0.875 at a recall level of 0.6 for our model. In contrast, the DeepIPN model performs better at higher recall levels, as detailed in Table S3. However, the DeepIPN struggles with the UCLA dataset, with the lowest AUROC of 0.624 and AUPRC of 0.601, alongside the highest FPR and the lowest precision across all recall levels. On the other hand, the CLIP model demonstrates the best FPR and precision across recall levels ranging from 0.6 to 0.8, as illustrated in Table S4.

In the DLCS, our model achieves the highest AUROC of 0.888, although it has a less favorable AUPRC of 0.393. Nevertheless, as shown in Table S5, across all recall levels from 0.6 to 0.9, the CLIP model maintains a lower FPR while demonstrating comparative or higher precision than Sybil and DeepIPN.

Table 2: Model Performance on Lung Cancer Prediction Within One Year. We conducted a comparative analysis of our model against three SOTA lung cancer risk assessment models, evaluating performance through AUROC and AUPRC scores on a held-out test set, as well as on three external datasets, each encompassing various types of CT scans and patient cohorts. Sybil and Venkadesh et al. models were not assessed on the NLST test set, as both models were trained on NLST. Performance of Venkadesh et al. on DLCS and UCLA could not be obtained due to data privacy and platform credits issues.

Models	NLST Test Set				External Datasets			
	NLST N=188 (56)		LUNGx 70 (35)		DLCS 1120 (63)		UCLA N = 51 (28)	
	AUROC	AUPRC	AUROC	AUPRC	AUROC	AUPRC	AUROC	AUPRC
Imaging Only Models								
Sybil	-	-	0.662	0.669	0.869	0.426	0.734	0.780
Venkadesh et al.	-	-	0.684	0.702	-	-	-	-
Imaging + Semantic Features Models								
DeepIPN	0.862	0.679	0.709	0.658	0.871	0.494	0.624	0.601
Ours (CLIP)	0.895	0.775	0.763	0.800	0.888	0.393	0.768	0.825

4.2. Model Explainability

We employ the inherent capacity of CLIP, zero-shot inference, to predict semantic features. Table 3 presents the performance metrics for general, internal, and external features. Our model demonstrates robust AUROC scores for general nodule features, including nodule margin (0.812), margin conspicuity (0.859), and consistency (0.812). Performance in predicting external features is fairly strong, with AUROC of 0.747 for vascular convergence, 0.840 for pleural attachment, and 0.756 for paracicatrial emphysema. However, the model struggles to predict most internal features, achieving notable results only for cyst-like spaces (0.731) and eccentric calcification (0.794).

Table 3: **Semantic Features Prediction Through Zero-shot Inference.** We presented a subset of the semantic features and their respective classes. We assessed the performance of predicting semantic features by using weighted AUROC for cases with multiple classes and standard AUROC for those with binary elements. For some of the features, the total percentage may not add up to 100% because of missing values. While the prediction shows solid performance in both general and external features, the internal features fail to provide satisfactory zero-shot inference results. This can be attributed to two main factors. First, internal features show a significant imbalance in their presence and absence. Second, the alignment between two modalities may be dominated by semantic features indicating malignancy.

Semantic Features	Classes (%)	AUROC
General Features		
Nodule Margin	Smooth (67) Lobulated (22) Spiculated (24) Ill-defined (19)	0.812
Nodule Consistency	Peri-cystic (2) Solid (73) Pure ground glass (9) Semiconsolidation (8) Part-solid (8)	0.812
Nodule Shape	Irregular (31) Ovoid (35) Polygonal (14) Round (19)	0.670
Nodule Margin Conspicuity	Well marginated (84) Poorly marginated (16)	0.859
Internal Features		
Nodule Reticulation	Present (88) Absent (12)	0.411
Cyst-like Spaces	Present (14) Absent (86)	0.731
Necrosis	Present (0.4) Absent (99.6)	0.112
Eccentric Calcification	Present (3) Absent (96)	0.794

Continued on next page

Table 3: Semantic Features Prediction Through Zero-shot Inference (continued).

Semantic Features	Classes (%)	AUROC
Cavitation	Present (0.4) Absent (99.6)	0.620
Intra-nodular bronchiectasis	Present (3) Absent (97)	0.425
Airway Cutoff	Present (2) Absent (27)	0.387
External Features		
Vascular Convergence	Present (10) Absent (89)	0.747
Pleural Retraction	Present (80) - Mild and Obvious Dimpling Absent (20)	0.689
Pleural Attachment	Present (53) Absent (47)	0.840
Paracapacitrial Emphysema	Present (12) Absent (88)	0.756
Septal Stretching	Present (69) Absent (30)	0.670

4.3. Ablation Studies

In Table 4, we present the mean and standard deviation of AUROC and AUPRC across five folds for various tuning methods and modalities. The CLIP model trained with LoRA performs better in predicting lung cancer risk than a model trained with fine-tuning and probing. Furthermore, with only the semantic features, the model achieves an AUROC of 0.888 and an AUPRC of 0.784, the highest among the three trained models. The CLIP model trained with semantic and imaging features outperforms the CLIP vision encoder trained with imaging data only across all datasets.

4.4. Error Analysis

In Figure 4, we present nodules of three lung cancer patients and three non-lung cancer patients, examining the predicted probabilities or risk scores generated by our CLIP and SOTA models.

Figures 4a and 4b depict non-cancerous cases, but our model assigns them notably high scores of 0.896 and 0.914, respectively. Even though biopsy results indicate a negative finding for the nodule in Figure 4a, it appears highly suspicious due to its large size, irregular shape, and spiculated margins. All other models also assign a high-risk score to this nodule. However, in Figure 4b, while the nodule appears lobulated and notched with irregular margins

Table 4: **Performance of Ablation Studies.** The first three rows display the outcome of the CLIP model, which was trained using various tuning methods. The last three rows display the performance of models trained on different modalities. The ^{*} superscript denotes a statistically significant difference in performance compared to the best-performing model. The logistic regression model, which was trained solely on semantic features, was not assessed on the external datasets due to the absence of semantic features.

Tuning Methods	NLST Test Set		LUNGx		External Datasets		UCLA	
	NLST N=188 (56)		70 (35)		DLCS 1120 (63)		N = 51 (28)	
	AUROC	AUPRC	AUROC	AUPRC	AUROC	AUPRC	AUROC	AUPRC
Training With Different Tuning Methods								
Fine-tuning	0.815 \pm 0.013 [*]	0.541 \pm 0.050 [*]	0.654 \pm 0.036 [*]	0.638 \pm 0.057 [*]	0.817 \pm 0.018 [*]	0.219 \pm 0.022 [*]	0.576 \pm 0.038 [*]	0.602 \pm 0.052 [*]
Probing	0.845 \pm 0.018	0.665 \pm 0.027	0.725 \pm 0.014	0.724 \pm 0.030	0.862 \pm 0.003	0.330 \pm 0.01	0.722 \pm 0.017	0.753 \pm 0.007
Ours(LORA)	0.885 \pm 0.011	0.758 \pm 0.017	0.762 \pm 0.014	0.799 \pm 0.020	0.879 \pm 0.007	0.358 \pm 0.027	0.743 \pm 0.028	0.799 \pm 0.020
Training With Different Modalities								
Logistic Regression (Semantic features only)	0.888 \pm 0.002	0.784 \pm 0.008	-	-	-	-	-	-
CLIP vision encoder (imaging features only)	0.811 \pm 0.031 [*]	0.593 \pm 0.050 [*]	0.683 \pm 0.033	0.716 \pm 0.035	0.813 \pm 0.019	0.279 \pm 0.030	0.664 \pm 0.042	0.689 \pm 0.032
Ours (CLIP)	0.885 \pm 0.011	0.758 \pm 0.017	0.762 \pm 0.014	0.799 \pm 0.020	0.879 \pm 0.007	0.358 \pm 0.027	0.743 \pm 0.028	0.799 \pm 0.020

and pleural retraction, DeepIPN accurately identifies the nodule as at lower risk. In Figure 4c, DeepIPN and Sybil return a relatively higher risk score. Still, our model accurately delivers a lower risk score for this negative case, which is characterized by its relatively small size and round shape.

Figures 4d and 4e illustrate two nodules diagnosed as lung cancer, yet our model underestimates the risk, providing relatively lower scores. Although both nodules are relatively small, they exhibit irregular shapes and mixed densities. Interestingly, the comparison models also predict low scores for these nodules. Finally, in Figure 4f, our model accurately outputs a high risk score to the malignant nodule, which is round and spiculated with septal stretching and vascular convergence, in contrast to the lower scores given by other models.

5. Discussion

In this study, we trained a CLIP model to align CT imaging features with semantic features to facilitate better lung cancer prediction. We preprocessed both image and semantic features to ensure alignment with the pre-trained CLIP format. To tackle the challenge of fine-tuning with a small dataset, we integrated LoRA and supervised branches into CLIP.

The performance of Sybil and Venkadesh et al. noticeably decreases when applied to the LUNGx dataset, which includes diagnostic and contrast-enhanced CT scans. This decrease can be attributed to the fact that both models were trained on the NLST dataset, which only contains LDCT, and the resulting distribution shift adversely impacted their performance. However, our model remains relatively robust even though we did not explicitly train on contrast-enhanced CT. In addition, our model demonstrates superior performance on the UCLA dataset, which consists of incidental nodules from non-smoking patients. Nevertheless, our model achieves the highest performance in terms of AUROC on the DLCS dataset but yields the lowest overall AUPRC. As shown in Table S5, our model demonstrates better performance comparable to that of DeepIPN and Sybil when focusing on higher recall levels. Our model outperforms SOTA models, showing consistent robustness across external datasets. In addition, by incorporating domain knowledge regarding the nodule characteristics, our model achieves performance comparable to or surpassing imaging-based SOTA models despite being trained on limited data. Our model utilized approximately 2,000 cases,

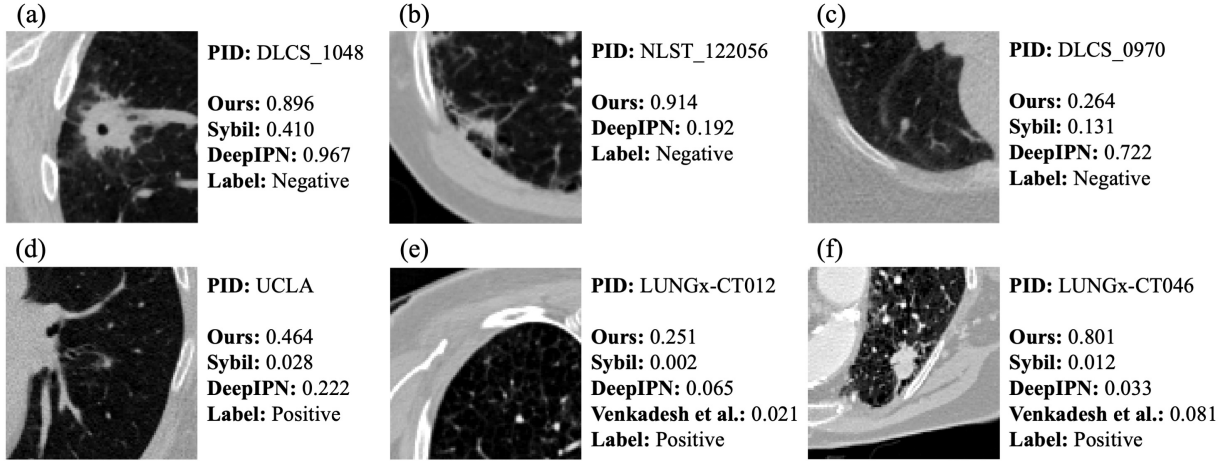


Figure 4: **Error Analysis.** Three malignant nodules (d-f) and three benign nodules (a-c) are presented. The risk scores generated from each model are displayed adjacent to the corresponding nodule images. The scale and range of the predicted probability or the risk score across different models can vary significantly. Since Sybil has performed calibration, the risk score is highly skewed to lower values. For example, in DLCS, Sybil has an interquartile range of 0.002–0.01, DeepIPN ranged from 0.05 to 0.21, and our model from 0.28 to 0.56. In LUNGx, Sybil ranged from 0.011 to 0.239, DeepIPN from 0.14 to 0.68, Venkadesh et al. from 0.14 to 0.68, and our model from 0.54 to 0.80.

whereas Sybil and Venkadesh et al. were trained on approximately 15,000 and 10,000 cases, respectively.

Our ablation study summarized in Table 4 shows high performance when we exclusively trained models on semantic features. This indicates that the semantic features utilized by radiologists to assess nodules were indeed indicative of the malignancy of those nodules. With the availability of semantic features, such a trained model can surpass imaging-based deep learning models in model performance and interpretability. Nonetheless, this approach may not be suitable for the clinical setting. First, we could not confirm its effectiveness and reliability on external datasets due to the absence of semantic features. Semantic feature annotations can be subjective, and radiologists can vary significantly. Further research is necessary to validate the robustness of the semantic features. Furthermore, implementing such a model in real-world settings would place an additional burden on radiologists as they would need to assess and document all of the semantic features for each nodule. On the other hand, even though the semantic features were utilized during training in CLIP, only CT images were required as input data at the inference stage. Considering the robustness of the model, our CLIP model possesses the potential for application across diverse clinical settings.

Training with the CT images themselves does not yield satisfactory results. However, our CLIP model demonstrates results comparable to those obtained by training solely with semantic features. This reveals that, guided by the semantic features in CLIP, the imaging features acquire clinically meaningful characteristics that correlate with the clinical features, resulting in enhanced model performance. Additionally, in a previous study [32], we investigated the characteristics and robustness of various imaging features by selecting prompts based on feature similarity for nodule segmentation in generalist foundation models. We

extracted imaging features from our CLIP model and compared these features against pixel intensity, radiomics features, and imaging biomarker foundation features for prompt selection. The results demonstrated that our CLIP feature-based prompt selection led to superior segmentation accuracy and robustness on external datasets. Given that the effectiveness of generalist segmentation models depends on the prompt examples, performing better when the prompt and test images exhibit similar semantics, backgrounds, and appearance, we can conclude that CLIP features are more effectively focusing on relevant nodule characteristics, indicating that the features from the CLIP imaging encoder are successfully aligned with nodule characteristics.

The zero-shot inference capability of the CLIP model improves model explainability, allowing our model to predict semantic features without requiring explicit training. Our model achieves high performance in predicting various general nodule characteristics, including margin, consistency, shape, and external features, such as pleural attachment and paracarcinomatous emphysema. This capability can aid clinicians in understanding the underlying meaning of model predictions. Nevertheless, predictions for other features, like nodule shape and most internal features, did not perform well. A well-known limitation of CLIP could cause the variability in zero-shot semantic feature prediction performance: its shortcomings in fine-grained alignment. In CLIP, global alignment is performed between multimodal features. Imaging and semantic features are converted into a single embedding and subsequently aligned. Therefore, it is likely that other semantic features have overshadowed certain features during training. Therefore, the local correspondences between different nodules or background regions and each semantic feature can be important in our particular case. In the future, our goal is to develop and validate the model further to facilitate more granular alignment. We hypothesize that this will aid the imaging feature model to learn more relevant clinical features.

Another limitation of our study lies in the preprocessing step. While we extracted nodules from nine distinct directions to preserve 3D characteristics to the greatest extent possible, certain features could still be overlooked during this process. Moreover, since our model focused exclusively on the nodule region, we did not include broader lung features like fibrosis and emphysema, which could also serve as risk factors for lung cancer. Furthermore, we did not evaluate the model developed by Venkadesh et al. on the DLCS and UCLA datasets due to limitations of running the model and sharing local data in a public, cloud environment.

6. Conclusion

We presented the benefits of integrating semantic features using the CLIP model, allowing the imaging encoder to learn more clinically significant and robust features. This model has achieved outstanding results in accurately predicting lung cancer risk across various external datasets, including patient cohorts and CT scan types. Additionally, our model offers explainability regarding nodule characteristics through zero-shot inference, which equips clinicians with better insights into how the model makes its predictions. Although the model was trained with semantic features, our model does not need manual annotation from radiologists, which enhances the model’s scalability. In summary, the model’s accuracy, robustness, explainability, and scalability underscore its promise for application in diverse clinical settings to facilitate the early detection of lung cancer.

CRediT authorship contribution statement

Luoting Zhuang: Writing - Original Draft, Writing - Review & Editing, Data Curation, Software, Methodology, Formal analysis, Visualization, Validation, Investigation, Conceptualization. **Seyed Mohammad Hossein Tabatabaei:** Data Curation, Writing – review & editing. **Ramin Salehi-Rad:** Data Curation, Writing – review & editing. **Linh M. Tran:** Data Curation, Writing – review & editing. **Denise Aberle:** Data Curation, Writing – review & editing, Funding acquisition, Conceptualization. **Ashley Prosper:** Data Curation, Writing – review & editing, Conceptualization. **William Hsu:** Data Curation, Writing – review & editing, Supervision, Project administration, Investigation, Funding acquisition, Conceptualization, Resources.

Declaration of competing interest

William Hsu reports funding support from the National Institutes of Health, Agency for Healthcare Research and Quality, Early Diagnostics Inc, personal fees from the Radiological Society of North America related to editorial board work, and consulting fees from LungLife AI, Inc. Ashley E. Prosper report funding support from the National Institutes of Health. Linh M. Tran reports funding support from the Department of Veterans Affairs Merit Review. If there are other authors, they declare that they have no known competing financial interests or personal relationships that could have appeared to influence the work reported in this paper.

Acknowledgments

We gratefully acknowledge the support of NIH/National Cancer Institute U2C CA271898 (to RSR, LMT, DA, AP, WH), U01 CA233370 (to LZ, DA, AP, WH), the V Foundation (to DA, WH), and the Department of Veterans Affairs Merit Review I01BX005721 (to LMT). The content is solely the responsibility of the authors and does not necessarily represent the official views of the National Institutes of Health.

Appendix A. Semantic Features Annotated

Table S1: Semantic Features Annotated by Radiologists for NLST Data.

Feature Type	Feature	Elements Contained
General features	longest axial diameter	3.7-62 mm
General features	short diameter	2-54 mm
General features	nodule consistency	Solid; Pure ground glass; Semiconsolidation; Part-solid; Peri-cystic
General features	nodule margin conspicuity	Well marginated; Poorly marginated

Feature Type	Feature	Elements Contained
General features	nodule margins	Spiculated/Serrated; Smooth; Lobulated; Ill-defined; Notched
General features	nodule shape	Ovoid; Round; Complex/Irregular; Polygonal
Internal features	nodule reticulation	Present; Absent
Internal features	cyst-like spaces	Present; Absent
Internal features	intra-nodular bronchiectasis	Present; Absent
Internal features	necrosis	Present; Absent
Internal features	cavitation	Present; Absent
Internal features	eccentric calcification	Present; Absent
Internal features	airway cut-off	Present; Absent
External features	pleural attachment	Present; Absent
External features	pleural retraction	Absent; Mild dimpling; Obvious dimpling
External features	vascular convergence	Present; Absent
External features	septal stretching	Present; Absent
External features	paracarcinomatous emphysema	Present; Absent
General Assessment	level of suspicion of lung cancer	Very Low; Moderately Low; Intermediate; Moderately High; High

Appendix B. False Positive Rate and Precision at a Given Recall.

Table S2: NLST Test Set.

Models	Recall ≈ 0.6		Recall ≈ 0.7		Recall ≈ 0.8		Recall ≈ 0.9	
	FPR \downarrow	Precision \uparrow						
DeepIPN	0.070	0.722	0.148	0.596	0.254	0.493	0.430	0.390
Ours (CLIP)	0.034	0.839	0.097	0.689	0.138	0.636	0.331	0.448

Table S3: LUNGx.

Models	Recall ≈ 0.6		Recall ≈ 0.7		Recall ≈ 0.8		Recall ≈ 0.9	
	FPR \downarrow	Precision \uparrow						
Sybil	0.229	0.724	0.543	0.568	0.743	0.519	0.914	0.500
Venkadesh et al.	0.371	0.618	0.571	0.568	0.600	0.571	0.771	0.542
DeepIPN	0.235	0.724	0.294	0.714	0.471	0.636	0.882	0.516
Ours (CLIP)	0.086	0.875	0.314	0.694	0.486	0.622	0.771	0.542

Table S4: **UCLA**.

Models	Recall ≈ 0.6		Recall ≈ 0.7		Recall ≈ 0.8		Recall ≈ 0.9	
	FPR \downarrow	Precision \uparrow						
Sybil	0.217	0.773	0.391	0.690	0.609	0.622	0.652	0.634
DeepIPN	0.304	0.708	0.609	0.588	0.609	0.622	0.783	0.591
Ours (CLIP)	0.174	0.810	0.174	0.833	0.522	0.657	0.826	0.578

Table S5: **DLCS**.

Models	Recall ≈ 0.6		Recall ≈ 0.7		Recall ≈ 0.8		Recall ≈ 0.9	
	FPR \downarrow	Precision \uparrow						
Sybil	0.087	0.313	0.149	0.230	0.344	0.131	0.442	0.109
DeepIPN	0.078	0.319	0.112	0.278	0.181	0.213	0.428	0.113
Ours (CLIP)	0.071	0.336	0.105	0.288	0.181	0.211	0.321	0.144

References

- [1] J. A. Barta, C. A. Powell, J. P. Wisnivesky, Global epidemiology of lung cancer, *Annals of global health* 85 (1) (2019) 8.
- [2] C. S. D. Cruz, L. T. Tanoue, R. A. Matthay, Lung cancer: epidemiology, etiology, and prevention, *Clinics in chest medicine* 32 (4) (2011) 10–1016.
- [3] N. L. S. T. R. Team, Reduced lung-cancer mortality with low-dose computed tomographic screening, *New England Journal of Medicine* 365 (5) (2011) 395–409.
- [4] H. J. de Koning, C. M. van Der Aalst, P. A. de Jong, E. T. Scholten, K. Nackaerts, M. A. Heuvelmans, J.-W. J. Lammers, C. Weenink, U. Yousaf-Khan, N. Horeweg, et al., Reduced lung-cancer mortality with volume ct screening in a randomized trial, *New England journal of medicine* 382 (6) (2020) 503–513.
- [5] J. R. Parikh, D. Wolfman, C. E. Bender, E. Arleo, Radiologist burnout according to surveyed radiology practice leaders, *Journal of the American College of Radiology* 17 (1) (2020) 78–81.
- [6] W. Wu, L. A. Pierce, Y. Zhang, S. N. Pipavath, T. W. Randolph, K. J. Lastwika, P. D. Lampe, A. M. Houghton, H. Liu, L. Xia, et al., Comparison of prediction models with radiological semantic features and radiomics in lung cancer diagnosis of the pulmonary nodules: a case-control study, *European radiology* 29 (2019) 6100–6108.
- [7] U. Bashir, B. Kawa, M. Siddique, S. M. Mak, A. Nair, E. Mclean, A. Bille, V. Goh, G. Cook, Non-invasive classification of non-small cell lung cancer: a comparison between random forest models utilising radiomic and semantic features, *The British journal of radiology* 92 (1099) (2019) 20190159.
- [8] P. G. Mikhael, J. Wohlwend, A. Yala, L. Karstens, J. Xiang, A. K. Takigami, P. P. Bourgouin, P. Chan, S. Mrah, W. Amayri, et al., Sybil: a validated deep learning model

to predict future lung cancer risk from a single low-dose chest computed tomography, *Journal of Clinical Oncology* 41 (12) (2023) 2191–2200.

- [9] K. V. Venkadesh, A. A. Setio, A. Schreuder, E. T. Scholten, K. Chung, M. M. W. Wille, Z. Saghir, B. van Ginneken, M. Prokop, C. Jacobs, Deep learning for malignancy risk estimation of pulmonary nodules detected at low-dose screening ct, *Radiology* 300 (2) (2021) 438–447.
- [10] L. Zhuang, A. Yadav, G. H. Kim, S. M. H. Tabatabaei, A. Prosper, W. Hsu, Exploring the impact of acquisition and reconstruction parameters on an imaging-based lung cancer risk model, in: 2024 46th Annual International Conference of the IEEE Engineering in Medicine and Biology Society (EMBC), IEEE, 2024, pp. 1–5.
- [11] N. Emaminejad, M. W. Wahi-Anwar, G. H. J. Kim, W. Hsu, M. Brown, M. McNitt-Gray, Reproducibility of lung nodule radiomic features: Multivariable and univariable investigations that account for interactions between ct acquisition and reconstruction parameters, *Medical physics* 48 (6) (2021) 2906–2919.
- [12] R. Geirhos, J.-H. Jacobsen, C. Michaelis, R. Zemel, W. Brendel, M. Bethge, F. A. Wichmann, Shortcut learning in deep neural networks, *Nature Machine Intelligence* 2 (11) (2020) 665–673.
- [13] A. J. DeGrave, J. D. Janizek, S.-I. Lee, Ai for radiographic covid-19 detection selects shortcuts over signal, *Nature Machine Intelligence* 3 (7) (2021) 610–619.
- [14] R. R. Selvaraju, M. Cogswell, A. Das, R. Vedantam, D. Parikh, D. Batra, Grad-cam: Visual explanations from deep networks via gradient-based localization, in: Proceedings of the IEEE international conference on computer vision, 2017, pp. 618–626.
- [15] S. Shen, S. X. Han, D. R. Aberle, A. A. Bui, W. Hsu, Explainable hierarchical semantic convolutional neural network for lung cancer diagnosis., in: CVPR workshops, 2019, pp. 63–66.
- [16] R. Gao, T. Li, Y. Tang, K. Xu, M. Khan, M. Kammer, S. L. Antic, S. Deppen, Y. Huo, T. A. Lasko, et al., Reducing uncertainty in cancer risk estimation for patients with indeterminate pulmonary nodules using an integrated deep learning model, *Computers in biology and medicine* 150 (2022) 106113.
- [17] L. Liu, Q. Dou, H. Chen, J. Qin, P.-A. Heng, Multi-task deep model with margin ranking loss for lung nodule analysis, *IEEE transactions on medical imaging* 39 (3) (2019) 718–728.
- [18] A. Radford, J. W. Kim, C. Hallacy, A. Ramesh, G. Goh, S. Agarwal, G. Sastry, A. Askell, P. Mishkin, J. Clark, et al., Learning transferable visual models from natural language supervision, in: International conference on machine learning, PMLR, 2021, pp. 8748–8763.
- [19] M. Christensen, M. Vukadinovic, N. Yuan, D. Ouyang, Vision–language foundation model for echocardiogram interpretation, *Nature Medicine* 30 (5) (2024) 1481–1488.

[20] X. Zhang, C. Wu, Y. Zhang, W. Xie, Y. Wang, Knowledge-enhanced visual-language pre-training on chest radiology images, *Nature Communications* 14 (1) (2023) 4542.

[21] Z. Huang, F. Bianchi, M. Yuksekgonul, T. J. Montine, J. Zou, A visual–language foundation model for pathology image analysis using medical twitter, *Nature medicine* 29 (9) (2023) 2307–2316.

[22] I. E. Hamamci, S. Er, F. Almas, A. G. Simsek, S. N. Esirgun, I. Dogan, M. F. Dasdelen, O. F. Durugol, B. Wittmann, T. Amiranashvili, et al., Developing generalist foundation models from a multimodal dataset for 3d computed tomography, *arXiv preprint arXiv:2403.17834* (2024).

[23] Y. Lei, Z. Li, Y. Shen, J. Zhang, H. Shan, Clip-lung: Textual knowledge-guided lung nodule malignancy prediction, in: *International Conference on Medical Image Computing and Computer-Assisted Intervention*, Springer, 2023, pp. 403–412.

[24] D. Aberle, Challenges in the semantic annotation of indeterminate nodules, in: *Society of Thoracic Radiology Annual Meeting*, San Diego, CA, 2025, keynote Speech.

[25] S. G. Armato III, G. McLennan, L. Bidaut, M. F. McNitt-Gray, C. R. Meyer, A. P. Reeves, B. Zhao, D. R. Aberle, C. I. Henschke, E. A. Hoffman, et al., The lung image database consortium (lidc) and image database resource initiative (idri): a completed reference database of lung nodules on ct scans, *Medical physics* 38 (2) (2011) 915–931.

[26] S. G. Armato III, K. Drukker, F. Li, L. Hadjiiski, G. D. Tourassi, R. M. Engelmann, M. L. Giger, G. Redmond, K. Farahani, J. S. Kirby, et al., Lungx challenge for computerized lung nodule classification, *Journal of Medical Imaging* 3 (4) (2016) 044506–044506.

[27] F. I. Tushar, A. Wang, L. Dahal, M. R. Harowicz, K. J. Lafata, T. D. Tailor, J. Y. Lo, Ai in lung health: Benchmarking detection and diagnostic models across multiple ct scan datasets, *arXiv preprint arXiv:2405.04605* (2024).

[28] G. Team, R. Anil, S. Borgeaud, J.-B. Alayrac, J. Yu, R. Soricut, J. Schalkwyk, A. M. Dai, A. Hauth, K. Millican, et al., Gemini: a family of highly capable multimodal models, *arXiv preprint arXiv:2312.11805* (2023).

[29] M. Ilse, J. Tomczak, M. Welling, Attention-based deep multiple instance learning, in: *International conference on machine learning*, PMLR, 2018, pp. 2127–2136.

[30] A. v. d. Oord, Y. Li, O. Vinyals, Representation learning with contrastive predictive coding, *arXiv preprint arXiv:1807.03748* (2018).

[31] E. J. Hu, Y. Shen, P. Wallis, Z. Allen-Zhu, Y. Li, S. Wang, L. Wang, W. Chen, et al., Lora: Low-rank adaptation of large language models., *ICLR* 1 (2) (2022) 3.

[32] L. Zhuang, S. M. H. Tabatabaei, D. R. Aberle, A. E. Prosper, W. Hsu, Comparing the characteristics and robustness of imaging features via prompt selection in generalist segmentation models, in: *Proc. of SPIE Vol*, Vol. 13411, 2025, pp. 134110Z–1.